This is the accepted (post-peer-review) version of the following article:

Ke, C.-Y., Chang, G. T., McLaskey, G. C., Kammer, D. S. & Marone, C. (2026) Nonlocal elastic unloading as a mechanism for breakdown work scaling in laboratory earthquakes. Earth and Planetary Science Letters, 693, 120283. https://doi.org/10.1016/j.epsl.2026.120283

Nonlocal Elastic Unloading as a Mechanism for Breakdown Work Scaling in Laboratory Earthquakes

Chun-Yu Ke[a,b,*], Gauss T. Chang[a], Gregory C. McLaskey[c], David S. Kammer[d], Chris Marone[b,e]

[a] *Department of Civil Engineering, National Taiwan University, Taipei, Taiwan*
[b] *Department of Geosciences, Pennsylvania State University, University Park, PA, USA*
[c] *School of Civil and Environmental Engineering, Cornell University, Ithaca, NY, USA*
[d] *Institute for Building Materials, ETH Zürich, Zürich, Switzerland*
[e] *Dipartimento di Scienze della Terra, La Sapienza Università di Roma, Roma, Italy*

Abstract

Understanding how earthquake energy budgets scale from laboratory to natural faults remains a fundamental challenge in earthquake physics. Laboratory experiments report fracture energies consistent with classical friction, yet seismological observations show that breakdown work scales strongly with slip, and the relationship between these two quantities remains unclear. Here we show that this discrepancy reflects two genuinely different physical quantities: the near-front dissipation governed by rupture-tip processes, which we use as a proxy for fracture energy because these small ruptures sustain no K-dominant field, and the system-scale breakdown work dominated by

*Corresponding author
Email address: chunyuke@ntu.edu.tw (Chun-Yu Ke)

nonlocal elastic unloading which includes the loading column in our experiments. We conducted stick-slip experiments on 15-cm long granite faults under normal stresses of 1–20 MPa in a double-direct-shear configuration. A dense strain-gauge array tracked rupture propagation, enabling near-front dissipation estimates via cohesive zone modeling, while finite element simulations quantified energy partitioning between the fault and loading system. The near-front dissipation remains low (<10 J/m^2) and scales roughly linearly with normal stress, consistent with classical friction. In contrast, total breakdown work scales quadratically with slip, exceeding the near-front dissipation by over an order of magnitude. Finite element simulations confirm that elastic unloading of the compliant loading column dominates this energy release. Normal stress heterogeneity on the lab fault produces additional weakening, after the rupture has reached maximum size, without additional dissipative mechanisms. These results demonstrate that apparent breakdown work scaling in laboratory earthquakes can arise from nonlocal elastic effects rather than intrinsic fault weakening. Our work provides a framework for distinguishing local near-front dissipation from system-scale energy release and breakdown work when extrapolating laboratory results to natural faults.

Keywords:
Rupture dynamics, Laboratory earthquakes, Breakdown work, Fracture energy

---

1. Introduction

Earthquake rupture reflects a dynamic redistribution of elastic strain energy within the fault–host rock system, balancing energy release from the surrounding medium against dissipation on and near the fault. This global energy flow governs the seismic stress drop and other source properties, including the rupture propagation speed C_f. Under suitable assumptions, this process can be formulated using linear elastic fracture mechanics (LEFM; Freund, 1990), in which rupture growth satisfies an energy balance $G = \Gamma$ between the dynamic energy release rate G and the fracture energy Γ (Kammer et al., 2024). In the context of LEFM, earthquake ruptures accelerate when the static energy release rate G_{II}^S (mode II) exceeds Γ (Svetlizky et al., 2020; Albertini et al., 2021).

Most experimental, analytical, and numerical studies have focused on the dissipative side of this balance, examining how rupture energy dissipation depends on slip rate, normal stress, fault roughness, and other weakening mechanisms (e.g., Cocco et al., 2006; Okubo et al., 2019; Kammer and McLaskey, 2019; Perry et al., 2020; Paglialunga et al., 2022; Cocco et al., 2023; Morad et al., 2024; Brantut, 2025). Far less attention has been given to the release side, namely, how the surrounding elastic medium unloads and transfers energy toward the rupture front. Yet this nonlocal energy supply can strongly influence rupture properties such as acceleration, total breakdown work, and their apparent dependence on normal stress.

Fault normal stress governs both sides of the fracture energy balance. Increasing normal stress enhances frictional strength and contact area (Dieterich and Kilgore, 1994), raising dissipation, but can also increase the elastic energy stored prior to rupture. In nature, ruptures at depth, where normal stress is high, tend to propagate faster than shallow or near-trench events (Vidale and Houston, 1993; Bilek and Lay, 2002). Laboratory experiments show the same trend: as normal stress increases, rupture speed increases (Johnson and Scholz, 1976; Leeman et al., 2016), approaching the Rayleigh or shear-wave velocity, and transitions to supershear rupture become more common (Xia, 2004; Dong et al., 2023). These observations point to a fundamental coupling between energy storage, release, and dissipation that governs rupture properties including speed.

In this study, we investigate small-scale laboratory earthquakes on a 15-cm long granite fault instrumented with a dense 13-station strain-gauge array. Our experiments enable spatially resolved measurements of rupture dynamics akin to those in larger, meter-scale experiments, but with additional control on loading rates and history. This allows us to reconstruct rupture fronts and estimate near-front dissipation locally, while we estimate breakdown work at the apparatus level, enabling comparison between local and system-wide energy dissipation. Because these ruptures are small, with a cohesive zone comparable to the fault length, the near-tip field is not K-dominated; we therefore report the local near-tip energy not as a strict fracture energy but as an apparent near-front dissipation Γ', a proxy for fracture energy obtained directly from the area under the initial weakening curve (Section 3.4). While the inferred near-front dissipation remains low, consistent with previous laboratory studies on single, relatively simple faults (e.g., Svetlizky et al., 2017; Bayart et al., 2015; Ke et al., 2018; Kammer and McLaskey, 2019; Paglialunga et al., 2022), total breakdown work increases strongly with normal stress (correlating with slip and stress drop), similar to trends observed in natural earthquakes (Cocco et al., 2023; Selvadurai, 2019; Viesca and Garagash, 2015; Abercrombie and Rice, 2005). We interpret this scaling not as a signature of increased fracture resistance and fracture energy, but as a consequence of greater energy release during elastic unloading of the fault and surrounding material including the loading column in our experiments. Our experiments demonstrate this for length-limited faults embedded in a compliant loading system, which is analogous to fault segments embedded in a damage zone or other cases where a small fault patch releases elastic energy stored in a larger volume. This analogy holds only in a restricted sense, for a fault patch of roughly fixed size, such as an asperity or fault segment embedded in a more compliant surrounding volume, for which the fixed dimension makes slip and stress drop co-vary. It is not a model for self-similar rupture growth, where the rupture dimension is not fixed and the stress drop is variable. The additional energy released as the fault completely unlocks arises from this elastic unloading, without requiring secondary weakening mechanisms (e.g., Gabriel et al., 2024; Lambert et al., 2021; Viesca and Garagash, 2015), and contributes to the observed scaling of breakdown work (e.g., Cocco et al., 2023; Abercrombie and Rice, 2005). These findings suggest that breakdown work scaling can be governed by system-scale elastic unloading rather than reflecting only the local weakening, offering a new perspective on energy partitioning in laboratory and natural earthquakes.

2. Methods

2.1. Experimental Setup

Friction experiments were conducted in the double-direct-shear (DDS) configuration using a biaxial load frame with adjustable loading stiffness (Leeman et al., 2016; Shreedharan et al., 2020). The samples consisted of a center block and two side blocks, all prepared from Barre Gray Granite, forming two 150 mm $\times$ 50 mm frictional interfaces (Fig. 1a). All edges of the center block and the top and bottom edges of the side blocks were chamfered 5 mm to reduce stress concentrations and prevent edge damage during repeated experiments. Throughout each experiment, normal load $\overline{\sigma_N}$ was held constant (force-controlled using a fast-acting servo system), while shear load $\overline{\tau}$ was applied through prescribed load-point velocities (using servo displacement control).

Along one of the 150 mm long faults (Fig. 1a), we installed 13 strain gauge rosettes to measure dynamic shear strain ε_{xy} at equally spaced locations, and normal strain ε_{yy} at 3 selected locations (x=3, 75, and 147 mm). The center of each strain gauge was located 8 mm from the fault. The dense array of ε_{xy} measurements enabled us to track the spatiotemporal onset of shear strain drop along the fault and estimate rupture speed (Fig. 1c) of laboratory earthquakes (labquakes). We used a servo-controlled loading sequence to produce 10's to 100's of labquakes in each experiment under the same conditions. Displacements at the load-point δ_{LP} and near the top of the center block δ (Fig. 1a, blue square), together with normal load $\overline{\sigma_N}$ and shear load $\overline{\tau}$, were recorded at 1 kHz, while dynamic strains were recorded separately at 100 kHz. The two systems measure independent quantities. The slow-sampling channels characterize system-level slip and stress while the strain gage array captures the dynamic rupture waveforms used for rupture speed and cohesive zone model fitting. Because the interseismic period between events is orders of magnitude longer than the rupture duration, events are unambiguously identified in both recording systems.

2.2. Sample Preparation and Testing Protocol

All experiments were conducted in the Rock Mechanics Laboratory at The Pennsylvania State University. We conducted experiments at normal loads $\overline{\sigma_N}$ ranging from 1 to 20 MPa, all following the same testing protocol. Before each experiment, the granite fault surfaces were roughened with #60 grit silicon-carbide (producing an RMS roughness of $\sim$20 μm) and a thin layer of

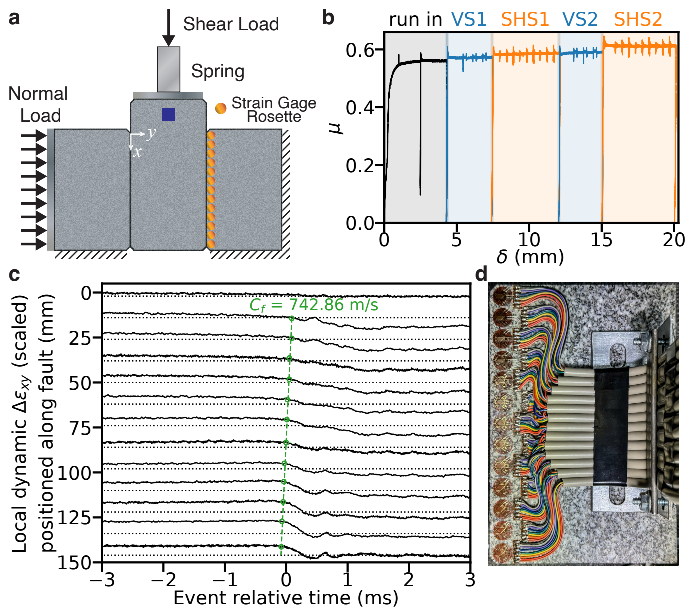

Figure 1: Double-direct shear experiment configuration. (a) Three Barre Gray granite blocks (two side blocks and one center block) are arranged under biaxial loading with bottom support for the two side blocks. Shear load is applied via an interchangeable loading block as a spring at the top of the center block. The right side block is instrumented with 13 strain gauge rosettes along the 150 mm fault. Blue square near the top of the center block marks the location of center block displacement δ measured relative to the bottom of the load frame. (b) Experimental protocol. Gray shading indicates the initial run-in phase in which the fault surfaces are conditioned prior to testing, blue shading indicates velocity-step tests (VS_i, stiff steel loading spring), and orange shading indicates slide-hold-slide tests (SHS_i, compliant acrylic loading spring). $\mu = \overline{\tau}/\overline{\sigma_N}$ is the friction coefficient and δ is center block displacement. (c) Dynamic shear strain ε_{xy} recorded at each strain gauge rosette along the fault, plotted as a function of time relative to the event onset. Horizontal dotted lines mark the zero strain change for each gauge trace. The topmost gauge did not record a rupture signal, likely because the rosette was too close to the top edge of the fault and was not in full contact with the fault surface. Green circles mark the onset of rupture at each gauge location; the green dashed line is fitted to these circles, and its slope gives the average rupture propagation speed. (d) A picture of the right side block, aligned to the strain gauge rosette positions shown in (c).

moisturized quartz powder (Min-U-Sil 40) was applied to each fault (~0.75 g; ~250 μm thick). This preparation procedure was adopted from Shreedharan et al. (2020) to achieve steady-state friction conditions and produce long sets of reproducible labquakes. As shown in Fig. 1b, the protocol included run-in, velocity-step (VS), and slide-hold-slide (SHS) tests. After applying normal stress, the center block was sheared to the load-point displacement of $\sim$5 mm, with an unload-reload cycle at $\sim$3 mm, to run in the faults. VS and SHS tests were then performed in alternating sequence (Fig. 1b) to assess cumulative strain effects, denoted VS_i and SHS_i according to their order. To generate reproducible labquakes with dynamic rupture, we used an acrylic block as a spring (80-mm long and 40x40 mm cross-sectional area) to reduce the loading stiffness and match the critical rate of frictional weakening K_c (e.g., Leeman et al., 2016; Scuderi et al., 2017). The acrylic block was used only for experiments at $<$ 15 MPa normal stress. It was installed after the initial run-in and VS tests to produce labquakes during SHS tests.

To verify that this sample exhibited frictional behavior comparable to previous experiments on the same apparatus with Westerly Granite (e.g., Leeman et al., 2016), we conducted VS tests to estimate rate-and-state friction parameters and K_c. The shear rate (load-point velocity) began at 10 μm/s, then alternated between 3 and 30 μm/s for three up-steps, with 500 μm of shear at each velocity. At normal loads above 7.5 MPa, we omitted VS tests because the fault did not sustain steady sliding and instead exhibited only stick-slip, precluding reliable rate-and-state fits. The estimated rate-and-state parameters (Supplementary Fig. S1) are consistent with those reported in previous works on Westerly granite and are therefore not discussed further.

SHS tests were used to induce dynamic rupture at low normal loads, where the conditions are otherwise in the stable sliding regime (Leeman et al., 2016; Pignalberi et al., 2024). Each SHS sequence comprised 3, 30, and 300 s holds, followed in each case by 500 μm of shear at 10 μm/s. Repeating the sequence 3 times produced 9 controlled stick-slip events per test. For consistency, we focus our detailed analysis on these 9 post-hold events, and use other events from our series of 15 tests to assess reproducibility and frictional behavior. At 15 and 20 MPa, we did not use the acrylic loading block (spring in Fig. 1a) because at these normal stresses the system satisfies the conditions for instability and exhibits stick-slip motion and labquakes. For each stick–slip event, we measured the total shear stress drop $\Delta\overline{\tau}_{\mathrm{total}}$, total slip δ_0, loading stiffness k taken from the linear segment of $\Delta\mu/\Delta\delta$ prior to failure, and the breakdown work $W_b = \int_0^{\delta_0} (\overline{\tau} - \overline{\tau}_{\mathrm{min}})\,\mathrm{d}\delta$, computed from the center-block displacement δ, shear load $\overline{\tau}$, and normal load $\overline{\sigma_N}$ (see Fig. 2).

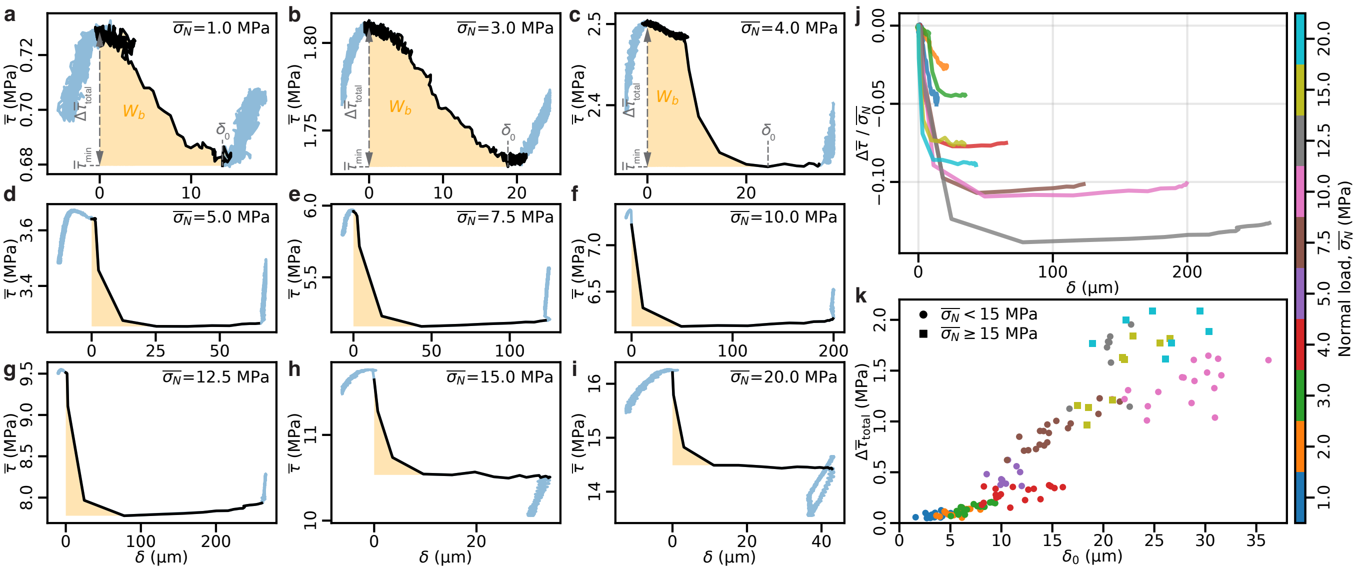

Figure 2: Dynamic stress drop and slip characteristics of laboratory earthquake events under different normal loads. (a–i) Shear load $\overline{\tau}$ versus fault displacement δ for events following SHS tests with 3-second holds, at $\overline{\sigma_N}$ from 1 to 20 MPa (the event at 2 MPa is excluded because of its similarity to the 1 and 3 MPa cases). Black sections denote the breakdown portion of stress drop, blue curves show the loading and post-slip history, and orange shading indicates breakdown work W_b, integrated from $\delta = 0$ to the displacement δ_0 at which $\overline{\tau}$ reaches its minimum $\overline{\tau}_{\text{min}}$ and breakdown ceases. The total stress drop $\Delta\overline{\tau}_{\text{total}}$, the weakening displacement δ_0, and the minimum shear stress $\overline{\tau}_{\text{min}}$ are marked in panels (a–c). (j) Normalized shear stress changes $\Delta\overline{\tau}$ from events (a–i) overlaid for comparison, including the 2 MPa event for completeness. (k) Total stress drop $\Delta\overline{\tau}_{\text{total}}$ versus weakening displacement δ_0 for all SHS events, where $\Delta\overline{\tau}_{\text{total}}$ is the difference in $\overline{\tau}$ between $\delta = 0$ and $\delta = \delta_0$. $\Delta\overline{\tau}_{\text{total}}$ and δ_0 show an overall linear relationship, with a small break for events with $\overline{\sigma_N} \geq 15$ MPa, where the loading stiffness was increased by removing the acrylic loading block (Fig. 1a).

2.3. Rupture Speed Estimation and Cohesive Zone Modeling

To estimate rupture speed, we first determine the rupture-front arrival time at each gauge location. The rupture front is conventionally identified with the peak in shear strain ε_{xy} (Svetlizky and Fineberg, 2014; Paglialunga et al., 2022). In our experiments, however, a distinct peak is not always present, because the fault length (150 mm) is comparable to the critical nucleation length ($h^{\star} \approx 0.5$ m in Ke et al., 2018; McLaskey, 2019), so the dynamic rupture often propagates through regions that are still actively nucleating and the characteristic peak is suppressed at those locations. We therefore define the rupture-front arrival as the onset of the rapid acceleration of the ε_{xy} drop (Ohnaka and Shen, 1999), which coincides with the peak where one is present and remains well defined where it is not. We developed an open-source Python GUI tool (Labquake Explorer; Ke, 2024) to pick rupture-front arrival times at each ε_{xy} measurement position. Arrival times and corresponding fault locations were then fit with linear regression to estimate rupture speed C_f, using positions near the fault center where velocity remained approximately constant (Fig. 1c).

Beyond rupture speed, characterizing the weakening process and fracture energetics requires fitting our dynamic strain measurements using the cohesive zone model, which regularizes the stress singularity inherent in LEFM (Paglialunga et al., 2022; Kammer and McLaskey, 2019; Poliakov et al., 2002; Samudrala et al., 2002). In this formulation, the dynamic stress/strain fields near the tip of a propagating mode II (in-plane shear) rupture are governed by the rupture speed C_f, fracture energy $\mathit{\Gamma}$, cohesive zone size X_c, and off-fault distance y. The near-tip stress change is given by Freund (1990)

$$\Delta\tau(\theta, r, C_f) = \frac{K_{II}(C_f)}{\sqrt{2\pi r}}\, \Sigma_{xy}^{II}(\theta, C_f), \tag{1}$$

where K_{II} is the mode-II stress intensity factor and Σ_{xy}^{II} its angular variation. The fracture energy $\mathit{\Gamma}$ is related to K_{II} through the dynamic energy release rate (Kammer and McLaskey, 2019)

$$\mathit{\Gamma} = G_{II} = \frac{1-\nu^2}{E}\, K_{II}^2\, f_{II}(C_f), \tag{2}$$

where $f_{II}(C_f)$ is a known universal function of crack speed. The cohesive zone introduces a linear slip-weakening stress distribution in local coordinates $\xi = x - x_{\text{tip}}$ (Poliakov et al., 2002; Samudrala et al., 2002)

$$\Delta\tau(\xi) = \begin{cases} 0, & \xi < -X_c \\ (1+\xi/X_c)(\tau_p - \tau_r), & -X_c < \xi < 0, \end{cases} \tag{3}$$

where τ_p and τ_r are the peak and residual shear stresses. Together Eqs. (1)–(3) predict the full $\Delta\tau(t)$ and $\Delta\varepsilon_{yy}(t)$ time histories at off-fault distance y. An example fit is shown in Fig. 3b–c.

The fitting window is chosen to isolate the local tip-weakening phase from the later system-scale unloading, as described below. Because the fault length is limited to 150 mm, the rupture front traverses the fault rapidly ($\sim$150 mm $\div$ 1 km/s = 0.15 ms), while reduction of τ persist with slip (Fig. 3b). This two-phase behavior reflects distinct energy release mechanisms: initial rapid weakening associated with local energy dissipation at the propagating rupture tip, followed by continued stress reduction driven by nonlocal elastic unloading of the fault blocks and loading column, including cases where the center block of the DDS arrangemenet undergoes nearly-rigid-body motion. This distinction is evident in Fig. 3d, where the initial drop in shear strain change $\Delta\varepsilon_{xy}$ propagates at a constant rate (green dashed line), whereas subsequent features appear nearly simultaneous across all locations in comparison (black dotted lines). To isolate the local rupture-tip energy dissipation from system-scale effects, we fit the cohesive zone model to only the initial weakening phase in $\Delta\varepsilon_{xy}$ and $\Delta\varepsilon_{yy}$ (Fig. 3b–c), while excluding the later features that represent nonlocal elastic unloading. For each event, we restricted the fits to the center gauge rosette ($x = 75$ mm), where both ε_{xy} and ε_{yy} are available, thereby enhancing the robustness of the fit. In the fitting procedure, we fix C_f based on estimates from multiple gauge rosettes and set $y = 8$ mm (fault to gauge center distance), then define the time window for the initial $\Delta\varepsilon_{xy}$ drop and jointly fit $\Delta\varepsilon_{xy}$ and $\Delta\varepsilon_{yy}$ for X_c and Γ (Supplementary Text S1).

3. Results and Discussion

3.1. Breakdown of Frictional Strength During Stick-Slip Events

We observe systematic changes in labquake characteristics over the normal stress range from 1–20 MPa (Fig. 2 and Supplementary Fig. S3). At $\overline{\sigma_N} < 4$ MPa, labquakes occurred only immediately after a hold, as the apparatus stiffness is slightly higher than K_c even with the acrylic loading block in place. In contrast, at $\overline{\sigma_N} \geq 4$ MPa (Fig. 2c–g), labquakes occurred repeatedly and $\Delta\overline{\tau}_{\text{total}}$ increased with δ_0 (Fig. 2k). Following the sudden drop, $\overline{\tau}$ remained at the residual level as δ increased, before rising again. This residual sliding phase appears to lengthen with increasing $\overline{\sigma_N}$ while the acrylic loading block is in place (Fig. 2j), but we note that for $\overline{\sigma_N} < 4$ MPa we do not observe residual, post-event sliding. For events at $\overline{\sigma_N} \geq 15$ MPa (Fig. 2h–i), where the apparatus stiffness is significantly higher, the center block of the DDS arrangement overshoots such that δ exceeds the product of event duration and prescribed load-point shear rate, which caused the servo system to retract and $\overline{\tau}$ to drop further (see blue segment near the end). The

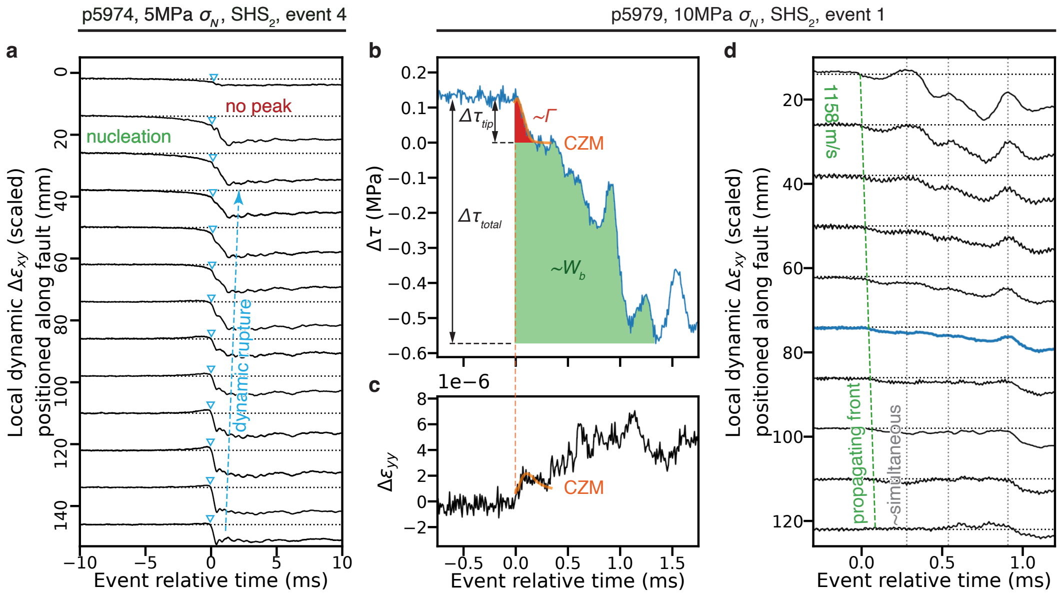

Figure 3: Dynamic strain records of lab earthquakes. (a) Shear strain change $\Delta\varepsilon_{xy}$ time history along the fault for one event with upward dynamic rupture propagation, selected because nucleation and dynamic propagation occur close enough in time to visualize both phases together. Rupture nucleates near $x = 20$ mm and quasi-statically propagates downward, loading the bottom of the fault near $x = 150$ mm, until dynamic rupture initiates at the bottom and propagates upward. Triangles mark the picked rupture-front arrival at each gauge. Note that at some locations, the dynamic strain records do not exhibit distinct peaks because the rupture front passes through regions that are still actively nucleating (see Section 2.3). Panels (b–d) show a second, separate event that initiates near the top and propagates downward. (b) Shear stress change $\Delta\tau = G\Delta\varepsilon_{xy}$ recorded by the strain gauge rosette at $x = 75$ mm. The trace is annotated with the local total stress drop $\Delta\tau_{\text{total}}$ (see panel d) and the stress drop at the rupture tip $\Delta\tau_{\text{tip}}$ obtained from the cohesive zone model (CZM, orange curve) fit. The red shaded area corresponds to the near-front dissipation Γ', while the green area (which includes Γ') corresponds to the breakdown work W_b. (c) Normal strain change $\Delta\varepsilon_{yy}$ recorded by the strain gauge rosette at $x = 75$ mm, as in (b). The trace agrees closely with the CZM fit (orange curve) within the fitted window and deviates afterward. Note that the sign of $\Delta\varepsilon_{yy}$ is opposite that of $\Delta\varepsilon_{xy}$, as expected for this geometry. (d) Shear strain change $\Delta\varepsilon_{xy}$ versus time at each gauge location along the fault. The blue curve at $x = 75$ mm corresponds to the trace shown in (b). The onset of shear strain drop propagates downward along the fault (green dashed line), while subsequent strain changes (black dotted lines) appear nearly simultaneous across all locations in comparison, indicating elastic waves generated by near-rigid-body motion of the center block.

stress-slip curve shows an inflection at the onset of the stress drop (visible in Fig. 2a–d), reflecting a two-stage weakening in which one fault begins to slide while the other remains locked briefly before both faults slip together (see Supplementary Fig. S4). Although this behavior can cause overestimation of W_b, the effect is more pronounced at lower $\overline{\sigma_N}$ and therefore does not significantly affect the derived scaling.

3.2. Experimental Scaling of Rupture Dynamics

Our labquakes reveal clear scaling relationships between fault rupture properties and the normal load $\overline{\sigma_N}$. Rupture propagation speed C_f increases systematically with increasing $\overline{\sigma_N}$, as shown in Fig. 4a. At the lowest $\overline{\sigma_N}$ (1–3 MPa), ruptures propagate slowly (a few hundred m/s), whereas at the highest $\overline{\sigma_N}$ (20 MPa), C_f reaches ∼1.8 km/s, which is still well below the Rayleigh-wave speed limit ($C_R \approx 2.5$ km/s). For an edge crack in a semi-infinite solid, the mode-II stress intensity factor scales as $K_{II}^S \propto \Delta\tau \propto \overline{\sigma_N}$ (Tada et al., 2000; Bayart et al., 2015; Ke et al., 2018), implying a static energy release rate

$$G_{II}^S \propto \overline{\sigma_N}^2. \tag{4}$$

Laboratory studies further suggest that fracture energy scales linearly with normal stress (Ke et al., 2018; Brodsky et al., 2020),

$$\mathit{\Gamma} \propto \overline{\sigma_N}. \tag{5}$$

Substituting these relations into the LEFM rupture speed expression (Svetlizky et al., 2017; Kammer et al., 2024),

$$C_f \approx \left(1 - \frac{\mathit{\Gamma}}{G_{II}^S}\right) C_R, \tag{6}$$

yields

$$C_f \propto 1 - \frac{c_0}{\overline{\sigma_N}}, \tag{7}$$

indicating that rupture speed should follow a hyperbolic approach to C_R as $\overline{\sigma_N}$ increases (dotted curve in Fig. 4a). In contrast, our data show only a modest acceleration with $\overline{\sigma_N}$, indicating that rupture speed cannot be explained by the standard LEFM scalings $G_{II}^S \propto \overline{\sigma_N}^2$ and $\mathit{\Gamma} \propto \overline{\sigma_N}$. This discrepancy has two potential explanations: 1) An additional mechanism beyond standard energy release: if G_{II}^S is treated as a quadratic function of $\overline{\sigma_N}$, i.e., $G_{II}^S = c_1\overline{\sigma_N}^2 + c_2\overline{\sigma_N}$ with fitting constants c_1 and c_2, the resulting form $C_f \propto 1 - 1/(c_1\overline{\sigma_N} + c_2)$ provides a much closer fit to our data (dashed curve in Fig. 4a). 2) The 150 mm fault length may not provide sufficient distance for ruptures to fully accelerate, particularly at higher $\overline{\sigma_N}$ where the potential C_f is greatest.

As shown in Fig. 4b, the total shear stress drop $\Delta\overline{\tau}_{\text{total}}$ increases with $\overline{\sigma_N}$, scaling approximately as $0.1\overline{\sigma_N}$, consistent with previous studies (e.g., Johnson and Scholz, 1976; Karner and Marone, 2000; Leeman et al., 2016; Dong et al., 2023; Lyu et al., 2019). Following Shreedharan et al. (2020, Fig. 1b), who systematically varied shear loading stiffness k, we also find that $\Delta\overline{\tau}_{\text{total}}$ is larger at lower k (Fig. 4c). The outlier cluster corresponds to experiments at $\overline{\sigma_N}$ of 15 and 20 MPa, where the loading stiffness was significantly higher in the absence of the acrylic loading block. These results indicate that the stress drop magnitude following complete fault unlocking is governed by the stiffness of the surrounding medium (which, in our case, includes the apparatus and shear loading column).

3.3. Breakdown Work Scaling

Breakdown work W_b follows power-law scaling with the weakening displacement δ_0, $W_b \propto \delta_0^2$ (Fig. 4d), consistent with patterns observed for natural earthquakes (Abercrombie and Rice, 2005; Viesca and Garagash, 2015; Cocco et al., 2023) and with laboratory measurements (Selvadurai, 2019). A best-fit power law with an exponent of 2 is consistent with scalings inferred for natural earthquakes (exponent range 0.67–2, Abercrombie and Rice, 2005; Cocco et al., 2023). The $\sim \delta_0^2$ scaling arises because $W_b \sim 0.5\Delta\overline{\tau}_{\text{total}}\delta_0$ and $\Delta\overline{\tau}_{\text{total}}$ scales approximately linearly with δ_0 (Fig. 2j). This quadratic dependence is a direct consequence of the fixed dimensions of our laboratory fault, where slip is limited by the elastic relaxation of the surrounding compliant system and stress drop and slip therefore co-vary. Natural ruptures are not dimension-limited in the same way, so slip and stress drop need not co-vary as they do here, and the quadratic scaling we measure should not be expected to carry over to them (Udías et al., 2014; Nielsen et al., 2016). In both cases the breakdown work is set by the elastic energy released from the volume surrounding the rupture rather than by frictional processes at the rupture tip. In our length-limited fault the fixed dimension couples slip to stress drop and yields an exponent of two, as it would for a fault patch of roughly fixed size, such as an asperity or fault segment embedded in a more compliant surrounding volume. This is not a model for self-similar rupture growth,

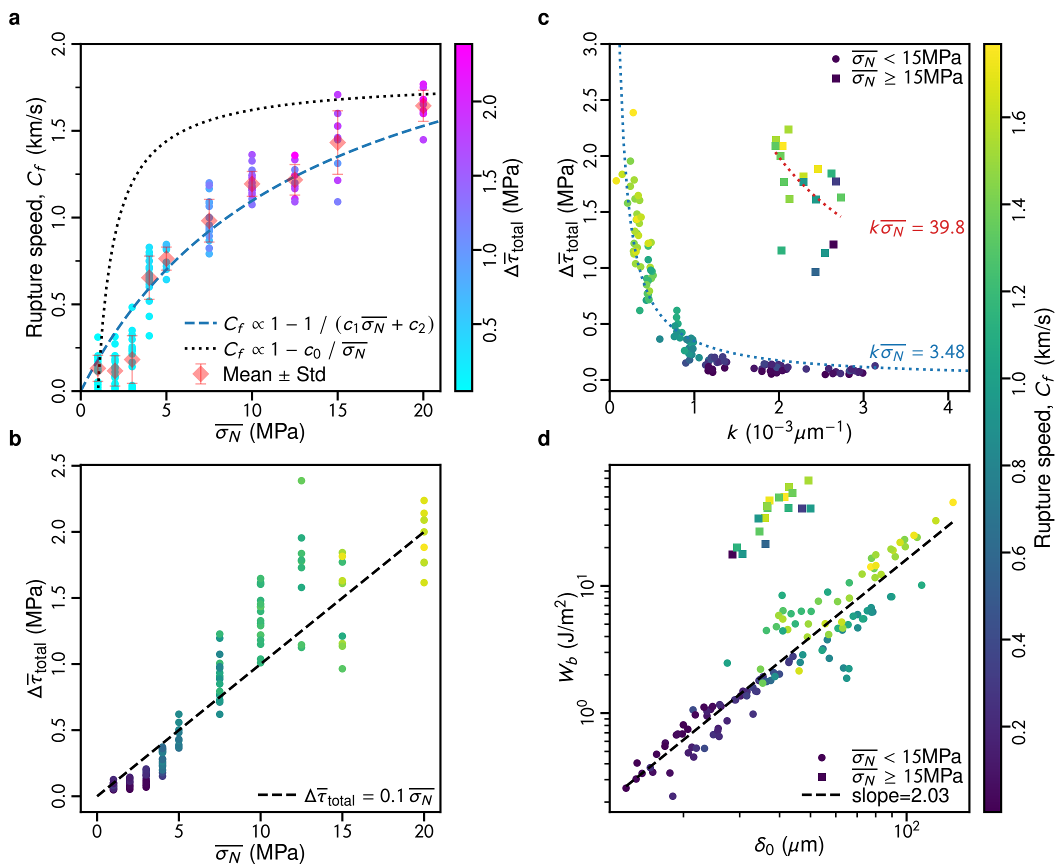

Figure 4: Scaling of rupture speed, stress drop, and breakdown work. (a) Rupture speed C_f increases systematically with normal stress $\overline{\sigma_N}$. The black dotted curve represents the fit $C_f \propto 1 - c_0/\overline{\sigma_N}$, while the dashed curve shows $C_f \propto 1 - 1/(c_1\overline{\sigma_N} + c_2)$. (b) Total stress drop $\Delta\overline{\tau}_{\mathrm{total}}$ increases with normal load, with $\Delta\overline{\tau}_{\mathrm{total}} \approx 0.1\overline{\sigma_N}$. (c) $\Delta\overline{\tau}_{\mathrm{total}}$ versus normalized loading stiffness k shows a trend similar to that reported by Shreedharan et al. (2020), with lower stiffness yielding higher stress drop. The outlier cluster corresponds to events at $\overline{\sigma_N} \geq 15$ MPa conducted with a much higher stiffness. The dotted and the dashed curves indicate constant values of the stress-per-displacement stiffness $\overline{k} = k\overline{\sigma_N}$ (in MPa/mm), following the scaling $\Delta\overline{\tau}_{\mathrm{total}} = 0.1\overline{\sigma_N} = 0.1\overline{k}/k$. (d) Breakdown work W_b scales with the weakening displacement δ_0 with an exponent of 2.03 (dashed line).

where the rupture dimension is not fixed and the stress drop is variable, so this nonlocal mechanism does not imply any single slip exponent, consistent with the broad range of exponents reported for natural earthquakes. In this restricted sense, laboratory faults with length-limited contacts reproduce key aspects of natural fault behavior inferred from seismology.

Previous larger-scale laboratory earthquake studies focus on rupture dynamics before the rupture spans the entire fault, and thus this post-rupture behavior has not been previously highlighted. In the DDS configuration, large ruptures produce complete unlocking and subsequent rigid block motion, which unloads both the fault-surrounding material and the shear loading column, thereby producing the strong W_b scaling.

3.4. Near-Tip Weakening from Cohesive Zone Modeling

The CZM (Section 2.3) fits well for the initial strain drop at the center rosette ($x = 75$ mm) and it captures near-tip weakening (Fig. 3b–c). The stress drop at the rupture tip $\Delta\tau_{\text{tip}}$ is significantly smaller than the total stress drop and shows little dependence on $\overline{\sigma_N}$ (Fig. 5a), though $\Delta\tau_{\text{tip}}$ is higher at lower $\overline{\sigma}_N$, likely reflecting increased uncertainty in distinguishing tip from tail behavior during fitting. The cohesive zone size X_c varies only weakly with $\overline{\sigma_N}$ (Fig. 5b), yet consistently exceeds the fault length. The cohesive zone model remains a valid elastic description of the near-tip strain fields, and X_c is a real length scale over which the rupture-front stresses evolve. However, because X_c is comparable to or larger than L, there is no region outside the cohesive zone yet close to the tip where the field is K-dominated. The small-scale yielding condition is therefore not satisfied, the fitted amplitude is an amplitude parameter of the solution rather than a true stress intensity factor, and X_c should not be read as a literal cohesive zone. Accordingly, we do not interpret the CZM-derived energy as a strict fracture energy. We instead report it as an apparent near-front dissipation scale $\mathit{\Gamma}'$, obtained as the area under the τ–δ curve during initial weakening. This area is constrained directly by the near-field gauge ($y \ll X_c$) and is insensitive to the assumed weakening-law shape, providing a robust measure of near-front dissipation for comparison with the breakdown work W_b. The two quantities are obtained independently, W_b from the finite-geometry energy budget and $\mathit{\Gamma}'$ from the near-field strain record, and neither relies on the small-scale-yielding assumption that fails here.

Our data show that the near-front dissipation $\mathit{\Gamma}'$ increases systematically with normal load (Fig. 5c). The scaling is roughly consistent with the fracture energy $\mathit{\Gamma} \approx 0.2\,\mu\text{m} \cdot \sigma_N$ reported by Ke et al. (2018), and our values are comparable in magnitude to previous studies (Svetlizky et al., 2017; Bayart et al., 2015; Ke et al., 2018; Kammer and McLaskey, 2019; Paglialunga et al., 2022). However, $\mathit{\Gamma}'$ remains an order of magnitude smaller than the breakdown work W_b (Ke et al., 2022), underscoring that much of the energy release occurs late in the process, after the rupture front has passed, after local stresses have dropped, and after the rupture has reached its final dimensions. Notably, events at $\overline{\sigma_N} \geq 15$ MPa conducted without the compliant loading spring fall above the $W_b \propto \delta_0^2$ trend (Fig. 4d, squares) because their stress drop is high relative to their slip, yet show no corresponding departure in Γ' at these same normal stresses (Fig. 5c). This indicates that the W_b scaling arises from nonlocal elastic unloading of the loading system rather than from enhanced energy dissipation at the rupture tip.

Recent high-velocity experiments show that rupture dynamics, particularly slip acceleration and system stiffness, can strongly influence both transient weakening and breakdown work (Liao et al., 2014; Chen et al., 2025). Chen et al. (2025) demonstrated that friction evolution during dynamic rupture systematically deviates from flash-heating predictions, with breakdown work scaling aligning with natural earthquakes when acceleration effects are considered. Similarly, Liao et al. (2014) found that slip-pulse loading produces lower breakdown work than constant-velocity tests despite more intense weakening, attributing this to acceleration-enhanced gouge production. These studies suggest that system configuration and loading history can fundamentally influence energy partitioning during dynamic slip, consistent with our observation that loading stiffness modulates W_b while leaving Γ' unchanged. This indicates that the excess energy release in our experiments arises from off-fault elastic unloading rather than enhanced dissipation at the rupture tip through mechanisms such as flash heating (Viesca and Garagash, 2015). These observations motivate finite-element analysis to further evaluate how the static energy release rate G_{II}^S is partitioned and how it scales with $\overline{\sigma_N}$.

3.5. Finite Element Modeling for Estimating Energy Release Rate Scaling

Typical LEFM applications for lab earthquake experiments (e.g., Kammer et al., 2015; Bayart et al., 2015; Ke et al., 2018; Paglialunga et al., 2022) assume that the rupture is embedded in an infinite solid or semi-infinite half-space. While these approximations provide useful first-order insights, the finite size of lab fault zones, and in particular the fact that our fault length is comparable to the nucleation dimension, motivates a more detailed analysis. To evaluate the energy budget of our labquakes, we developed a finite element model in ABAQUS (Dassault Systèmes Simulia Corp., 2024), including the three granite blocks used for DDS, the steel plate on top of the center block

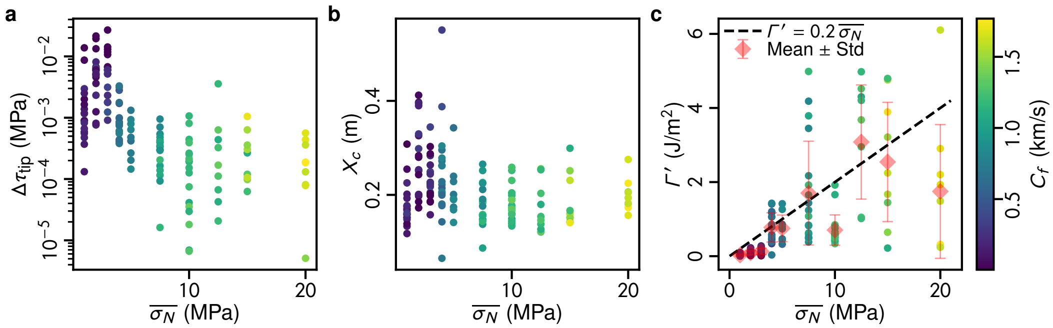

Figure 5: Cohesive-zone-model (near-tip) scaling. (a) Stress drop at the rupture tip $\Delta\tau_{\rm tip}$, estimated from CZM fits, decreases slightly with $\overline{\sigma_N}$ and is considerably smaller than the total stress drop $\Delta\overline{\tau}_{\rm total}$. (b) Cohesive zone size X_c shows little dependence on $\overline{\sigma_N}$ but mostly exceeds the 0.15 m fault length. (c) Near-front dissipation Γ' dependence on $\overline{\sigma_N}$ is broadly consistent in magnitude with the fracture-energy scaling $\Gamma \approx 0.2\mu{\rm m}\cdot\sigma_N$ reported by Ke et al. (2018, dashed line).

for stress distribution, and the acrylic block used to reduced loading stiffness for lower normal stress (Fig. 6).

Because our shear loading rate is negligible relative to the dynamic rupture speed, we prescribe a displacement at the top of the DDS loading column and gradually increase the rupture area in static steps by varying the rupture length a, assuming the rupture front is uniform across the fault width. The rupture area is simulated by frictional contact with $\mu = 0.7$, whereas the unruptured regions are tied together with a zero-relative-displacement boundary condition. Although this model does not capture the full dynamics of rupture propagation, it provides a first-order framework for evaluating the validity of LEFM assumptions in our experimental system and for estimating how G_{II}^S scales with σ_N.

We ran simulations ranging from $\overline{\sigma_N}$ from 2.5 to 20 MPa, and for each normal load considered rupture lengths a from 5 to 105 mm, assuming symmetric rupture on both frictional interfaces. The energy release rate was computed as $G^{S\prime} = -{\rm d}U/{\rm d}A$ using a central-difference approximation, where U is the total strain energy, $A = aw$ is rupture area, and $w = 50$ mm is the fault width. For comparison with the experiments, we take $G^{S\prime}$ at $a = 75$ mm (rupture front at fault center) as the representative value for each normal stress (Fig. 6e).

The simulations show that the loading column with the acrylic block

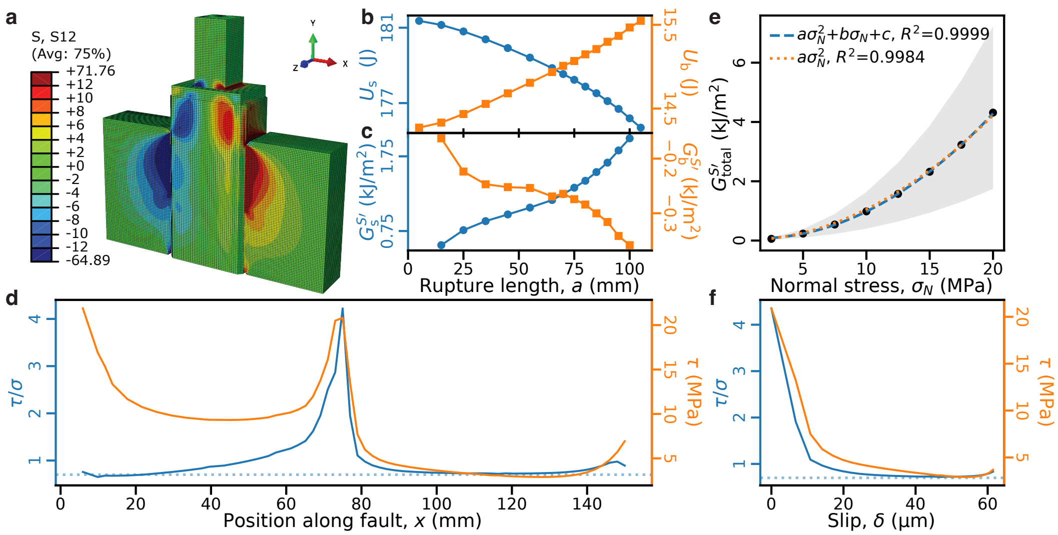

Figure 6: Finite element model results for a bottom-up rupture. (a) Shear stress field along the fault direction τ in the 3D finite element model. S12 denotes shear stress σ_{xy} in the model. (b) Strain energy stored in the acrylic spring U_s (blue) and in the granite blocks U_b (orange) as a function of rupture length a. (c) Energy release rate from the acrylic spring $G_s^{S\prime}$ (blue) and from the granite blocks $G_b^{S\prime}$ (orange) as a function of a. (d) Spatial distribution of the shear-to-normal stress ratio τ/σ_N (blue) and shear stress τ (orange) at a rupture length of 75 mm. Dashed line shows the prescribed target friction coefficient. (e) Total static energy release rate $G^{S\prime}$ as a function of $\overline{\sigma_N}$, overlaid with a quadratic polynomial fit (blue dashed) and a pure quadratic fit (orange dotted). The gray shaded area marks the range of $G^{S\prime}$ for rupture lengths $a \in [15, 100]$ mm (as shown in c), and the black dots indicate $a = 75$ mm. (f) Shear-to-normal stress ratio τ/σ_N (blue) and shear stress τ (orange) versus slip δ for $\delta > 0$ at all fault nodes at a rupture length of 75 mm. Dashed line indicates the prescribed target friction coefficient. See Supplementary Fig. S2 for the top-down rupture case.

stores more than an order of magnitude more strain energy than the granite blocks (Fig. 6b). The corresponding energy release rates exhibit the same partitioning, with $G_s^{S\prime}$ denoting energy released from the loading column (subscript s) and $G_b^{S\prime}$ from the granite blocks (subscript b) (Fig. 6c). Interestingly, the strain energy in the granite blocks increases with rupture area ($A = aw$) rather than releasing energy ($G_b^{S\prime} < 0$, Fig. 6c) —*i.e.*, the blocks continue to store energy as rupture grows. This behavior arises because reduced lateral restraint from the side blocks permits greater deformation of the center block as rupture area expands. Thus, even though strain energy is released at the rupture tips, the total strain energy of the blocks increases.

In the case with top-down rupture, the energy release rate in the two side blocks is positive (Supplementary Fig. S2), as expected, but remains considerably lower than the energy release rate from the loading column with the acrylic block ($G_s^{S\prime}$). These results confirm that elastic energy release from the loading column, rather than localized rupture-tip processes, governs the energy budget in our laboratory earthquakes, and that this energy release begins even before the rupture spans the entire fault and rigid-body motion of the center block commences.

At a representative rupture length of $a = 75$ mm, the total energy release rate ($G_{\mathrm{total}}^{S\prime}$) increases quadratically with $\overline{\sigma_N}$ (Fig. 6e), showing no deviation from the simplified LEFM prediction $G_{II}^{S} \propto \overline{\sigma_N}^2$ (curves in Fig. 6e), despite the geometric and compositional complexity of our experimental setup. Notably, because $G^{S\prime}$ is computed directly from the finite-geometry energy budget rather than from a stress intensity factor, this agreement does not rely on small-scale yielding (cf. Palmer and Rice, 1973). We write $G^{S\prime}$, with a prime as for the apparent near-front dissipation Γ', to denote a finite-geometry energy release rate determined without a K-dominant field. The quadratic scaling is therefore robust rather than an artifact of the small-scale-yielding assumption underlying the analytical prediction, and it persists beyond the small-scale-yielding regime. Our finite-element model is static and is not intended to reproduce the rupture speed. It therefore does not capture the modest deviation of C_f from $C_f \propto 1 - c_0/\overline{\sigma_N}$ (Fig. 4a). Reproducing that deviation would likely require fully dynamic simulations with a friction law. Importantly, this deviation concerns only the rupture speed. It does not bear on our energy-budget analysis, from which we conclude that the breakdown-work scaling arises from system-scale elastic unloading.

Beyond the energy release rate scaling, the finite-element model also reveals how spatial heterogeneity in normal stress affects fault behavior. Due to the finite geometry of our experimental setup, σ_N varies spatially along the fault. This heterogeneity causes τ and τ/σ_N to exhibit markedly different spatial patterns, with τ showing pronounced stress concentrations near rupture tips while τ/σ_N remains more uniform (Fig. 6d). During slip, these spatial variations in σ_N evolve, producing different slip-weakening behavior for the two quantities (Fig. 6f). Notably, $\tau(\delta)$ exhibits secondary weakening, a gradual stress decrease following the initial sharp drop, that is much less pronounced in $\tau/\sigma_N(\delta)$. This occurs because the evolving σ_N distribution produces curved τ-δ behavior even when the friction coefficient μ remains uniform. Consequently, interpreting the measured τ under the implicit assumption of a constant $\overline{\sigma_N}$, as is common in experimental studies, can overestimate fracture energy $\mathit{\Gamma}$ by misattributing this curvature to enhanced dissipation at the rupture tip (e.g., Cowie and Scholz, 1992). Thus, system-scale elastic unloading and finite-geometry effects can mimic signatures of complex weakening mechanisms, contributing to the observed breakdown work scaling without requiring additional energy dissipation near the rupture front.

3.6. Energy partitioning and the fault thermal budget

A natural question is where the released elastic energy ends up, and whether the strong scaling of breakdown work implies correspondingly strong frictional heating and thermally enhanced weakening on the fault (e.g., Nielsen et al., 2021; Cocco et al., 2023). While we do not measure temperature directly, mechanical work done against friction is expected to be largely converted to heat (Aretusini et al., 2021, 2024; Ortega-Arroyo et al., 2025), so most of the released energy likely ends up as frictional heat on the fault. Taking an event at $\overline{\sigma_N} = 20$ MPa as an example, the work done against friction is $\int \overline{\tau}\, \mathrm{d}\delta \approx \overline{\tau}\, \delta \approx 6 \times 10^2\ \mathrm{J\,m^{-2}}$, and the breakdown work $W_b = \int (\overline{\tau} - \overline{\tau}_{\min})\, \mathrm{d}\delta$ is the roughly ten percent of this work done above the minimum sliding stress (Fig. 4d). The near-front dissipation $\mathit{\Gamma}' \approx 10\ \mathrm{J\,m^{-2}}$, the energy dissipated locally during the initial weakening at the onset of slip, is smaller still. How W_b itself partitions among additional fault heating, kinetic energy of the near-rigidly translating center block (Fig. 3d), and radiated waves is not directly constrained by our measurements, but each of these sinks is modest. Spread through the $\sim$0.75 g gouge layer, the total frictional heat corresponds to a temperature rise of only $\Delta T = \overline{\tau}\, \delta\, A/(m\, c) \approx 8$ K, where A is the fault area, m is the gouge mass, and $c \approx 750\ \mathrm{J\,kg^{-1}\,K^{-1}}$ is the specific heat of quartz. This is two orders of magnitude below the rises required to activate flash heating, thermal pressurization, or melting (e.g., Viesca and Garagash, 2015; Harbord et al., 2021), so enhanced thermally activated weakening is neither expected nor observed. The scaling of W_b therefore does not indicate that rupture requires more energy to propagate, which is the role of $\mathit{\Gamma}$. It indicates that the surrounding system, including the loading column, releases more energy as the fault unlocks, energy that ends up as modest heat, radiated waves, and kinetic energy.

3.7. Implications for Natural Faults

Our finding that nonlocal elastic unloading governs the breakdown work scaling invites comparison with natural faults. Strong breakdown work scaling with earthquake size is inferred from seismology (Abercrombie and Rice, 2005; Tinti et al., 2005) and is commonly attributed to enhanced near-fault weakening such as thermal pressurization (Viesca and Garagash, 2015; Wibberley and Shimamoto, 2005). Our results point to an alternative, in which fault areas surrounding a high-strength asperity, though not in direct contact, store and release the elastic energy that drives this scaling. In this view, a finite-length laboratory fault embedded in a compliant loading system is analogous to a small asperity embedded in a larger elastic medium, where nonlocal unloading rather than enhanced weakening produces the scaling. Such an effect would be absent from laboratory and numerical models that assume perfectly mated fault interfaces. Our data therefore suggest that accounting for fault topography and contact heterogeneity, alongside frictional properties, may be essential for scaling rupture energetics from the laboratory to tectonic faults.

4. Conclusions

Our laboratory stick–slip experiments reveal that rupture speed C_f, stress drop $\Delta\overline{\tau}_{\text{total}}$, and breakdown work W_b scale systematically with normal load $\overline{\sigma_N}$. While these data are consistent with basic expectations they are not fully aligned with standard assumptions of LEFM. Although the near-front dissipation $\mathit{\Gamma}'$ grows approximately linearly with $\overline{\sigma_N}$, it remains an order of magnitude smaller than W_b, indicating that most energy release arises from system-scale unloading, after the rupture has reached the fault boundaries. This later slip is due to energy release of the shear loading column rather than from localized weakening at the rupture tip. Finite-element analysis shows that the static energy release rate $G_{\text{II}}^{S\prime}$ follows the quadratic scaling predicted by LEFM despite the geometric complexity of the experimental setup, while also revealing that the compliant loading column dominates the energy budget even before full sliding occurs. Cohesive zone modeling further indicates that the cohesive zone size X_c exceeds the sample dimensions, violating the small-scale yielding assumption even though the model fits the dynamic strain data reasonably well.

Our results highlight the role of finite, length-limited fault patches in governing rupture energetics. Together, these results identify nonlocal elastic unloading of the loading system, rather than enhanced near-tip dissipation, as the primary control on the breakdown-work scaling we observe.

CRediT authorship contribution statement

C.-Y. Ke: Writing - original draft, Methodology, Software, Validation, Formal analysis, Investigation, Data Curation, Visualization, Supervision, Project administration, Conceptualization, Funding acquisition. **G. T. Chang:** Software, Formal analysis, Data Curation, Visualization. **G. C. McLaskey:** Writing - review & editing, Validation, Resources, Conceptualization. **D. S. Kammer:** Writing - review & editing, Validation, Conceptualization. **C. Marone:** Writing - review & editing, Validation, Investigation, Resources, Supervision, Project administration, Conceptualization, Funding acquisition.

Declaration of competing interest

The authors declare that they have no known competing financial interests or personal relationships that could have appeared to influence the work reported in this paper.

Acknowledgements

The lab work was supported by European Research Council Advanced Grant 835012 (TECTONIC). C.-Y. K. gratefully acknowledges support from the National Science and Technology Council, Taiwan (NSTC 113-2116-M-002-031-MY3), the Yushan Fellow Program of the Ministry of Education (MOE), Taiwan (NTU-113V1045-1), and the Garmin Scholar Program at National Taiwan University, funded by the Kao Family Foundation. G.C.M. acknowledges support from the US National Science Foundation Grant EAR-2240375. The successful completion of this research was made possible by the academic resources and advanced research infrastructure provided by the National Center for High-Performance Computing, National Institutes of Applied Research (NIAR), Taiwan. We gratefully acknowledge their invaluable support. We thank the editor and two anonymous reviewers for their thoughtful and constructive comments, which greatly improved the manuscript.

Supplementary materials

Supplementary material associated with this article can be found, in the online version, at https://doi.org/10.1016/j.epsl.2026.120283.

Data availability

Data will be made available on request.

References

Abercrombie, R.E., Rice, J.R., 2005. Can observations of earthquake scaling constrain slip weakening? Geophysical Journal International 162, 406–424. URL: https://academic.oup.com/gji/article-lookup/doi/10.1111/j.1365-246X.2005.02579.x, doi:10.1111/j.1365-246X.2005.02579.x. arXiv: 1011.1669v3 ISBN: 0956-540X.

Albertini, G., Lebihain, M., Hild, F., Ponson, L., Kammer, D.S., 2021. Effective Toughness of Heterogeneous Materials with Rate-Dependent Fracture Energy. Physical Review Letters 127, 035501. URL: https://link.aps.org/doi/10.1103/PhysRevLett.127.035501, doi:10.1103/PhysRevLett.127.035501.

Aretusini, S., Nuñez Cascajero, A., Cornelio, C., Barrero Echevarria, X., Spagnuolo, E., Tapetado, A., Vazquez, C., Di Toro, G., Cocco, M., 2024. Mechanical Energy Dissipation During Seismic Dynamic Weakening in Calcite-Bearing Faults. Journal of Geophysical Research: Solid Earth 129, e2024JB028927. URL: https://agupubs.onlinelibrary.wiley.com/doi/10.1029/2024JB028927, doi:10.1029/2024JB028927.

Aretusini, S., Núñez-Cascajero, A., Spagnuolo, E., Tapetado, A., Vázquez, C., Di Toro, G., 2021. Fast and Localized Temperature Measurements During Simulated Earthquakes in Carbonate Rocks. Geophysical Research Letters 48, e2020GL091856. URL: https://agupubs.onlinelibrary.wiley.com/doi/10.1029/2020GL091856, doi:10.1029/2020GL091856.

Bayart, E., Svetlizky, I., Fineberg, J., 2015. Fracture mechanics determine the lengths of interface ruptures that mediate frictional motion. Nature Physics 12, 166–170. URL: http://www.nature.com/doifinder/10.1038/nphys3539, doi:10.1038/nphys3539.

Bilek, S.L., Lay, T., 2002. Tsunami earthquakes possibly widespread manifestations of frictional conditional stability. Geophysical Research Letters 29. URL: https://agupubs.onlinelibrary.wiley.com/doi/10.1029/2002GL015215, doi:10.1029/2002GL015215.

Brantut, N., 2025. Analysis of Stress in the Cohesive Zone, Dissipation and Fracture Energy During Shear Rupture Experiments. Geophysical Research Letters 52, e2024GL113972. URL: https://agupubs.onlinelibrary.wiley.com/doi/10.1029/2024GL113972, doi:10.1029/2024GL113972.

Brodsky, E.E., McLaskey, G.C., Ke, C., 2020. Groove Generation and Coalescence on a Large-Scale Laboratory Fault. AGU Advances 1. URL: https://onlinelibrary.wiley.com/doi/10.1029/2020AV000184, doi:10.1029/2020AV000184.

Chen, X., Saber, O., Chester, F.M., 2025. Velocity Dependence of Dynamic Rock Friction Modulated by Dynamic Rupture in High-Speed Friction and Stick-Slip Tests. Journal of Geophysical Research: Solid Earth 130, e2024JB030402. URL: https://agupubs.onlinelibrary.wiley.com/doi/10.1029/2024JB030402, doi:10.1029/2024JB030402.

Cocco, M., Aretusini, S., Cornelio, C., Nielsen, S.B., Spagnuolo, E., Tinti, E., Di Toro, G., 2023. Fracture Energy and Breakdown Work During Earthquakes. Annual Review of Earth and Planetary Sciences 51, 217–252. URL: https://www.annualreviews.org/content/journals/10.1146/annurev-earth-071822-100304, doi:10.1146/annurev-earth-071822-100304.

Cocco, M., Spudich, P., Tinti, E., 2006. On the mechanical work absorbed on faults during earthquake ruptures. Geophysical Monograph Series 170, 237–254. doi:10.1029/170GM24. iSBN: 9781118666272.

Cowie, P.A., Scholz, C.H., 1992. Physical explanation for the displacement-length relationship of faults using a post-yield fracture mechanics model. Journal of Structural Geology 14, 1133–1148. URL: https://linkinghub.elsevier.com/retrieve/pii/0191814192900655, doi:10.1016/0191-8141(92)90065-5.

Dassault Systèmes Simulia Corp., 2024. Abaqus 2024 Documentation. Technical Report. Dassault Systèmes. Johnston, RI, USA. URL: https://www.3ds.com/products-services/simulia/products/abaqus/.

Dieterich, J.H., Kilgore, B.D., 1994. Direct observation of frictional contacts: New insights for state-dependent properties. pure and applied geophysics

143, 283–302. URL: https://link.springer.com/10.1007/BF00874332, doi:10.1007/BF00874332.

Dong, P., Xia, K., Xu, Y., Elsworth, D., Ampuero, J.P., 2023. Laboratory earthquakes decipher control and stability of rupture speeds. Nature Communications 14, 2427. URL: https://www.nature.com/articles/s41467-023-38137-w, doi:10.1038/s41467-023-38137-w.

Freund, L.B., 1990. Dynamic Fracture Mechanics. volume 25. Cambridge University Press, Cambridge. URL: http://ebooks.cambridge.org/ref/id/CBO9780511546761, doi:10.1017/CBO9780511546761. arXiv: 1011.1669v3 Publication Title: Cambridge University Press Issue: 9.

Gabriel, A.A., Garagash, D.I., Palgunadi, K.H., Mai, P.M., 2024. Fault size–dependent fracture energy explains multiscale seismicity and cascading earthquakes. Science 385, eadj9587. URL: https://www.science.org/doi/10.1126/science.adj9587, doi:10.1126/science.adj9587.

Harbord, C., Brantut, N., Spagnuolo, E., Di Toro, G., 2021. Fault Friction During Simulated Seismic Slip Pulses. Journal of Geophysical Research: Solid Earth 126, e2021JB022149. URL: https://agupubs.onlinelibrary.wiley.com/doi/10.1029/2021JB022149, doi:10.1029/2021JB022149.

Johnson, T.L., Scholz, C.H., 1976. Dynamic properties of stick-slip friction of rock. Journal of Geophysical Research 81, 881–888. URL: http://doi.wiley.com/10.1029/JB081i005p00881, doi:10.1029/JB081i005p00881.

Kammer, D.S., McLaskey, G.C., 2019. Fracture energy estimates from large-scale laboratory earthquakes. Earth and Planetary Science Letters 511, 36–43. URL: https://doi.org/10.1016/j.epsl.2019.01.031, doi:10.1016/j.epsl.2019.01.031.

Kammer, D.S., McLaskey, G.C., Abercrombie, R.E., Ampuero, J.P., Cattania, C., Cocco, M., Dal Zilio, L., Dresen, G., Gabriel, A.A., Ke, C.Y., Marone, C., Selvadurai, P.A., Tinti, E., 2024. Earthquake energy dissipation in a fracture mechanics framework. Nature Communications 15, 4736. URL: https://www.nature.com/articles/s41467-024-47970-6, doi:10.1038/s41467-024-47970-6.

Kammer, D.S., Radiguet, M., Ampuero, J.P., Molinari, J.F., 2015. Linear Elastic Fracture Mechanics Predicts the Propagation Distance of Frictional Slip. Tribology Letters 57, 23–23. URL: http://link.springer.com/10.1007/s11249-014-0451-8, doi:10.1007/s11249-014-0451-8. arXiv: 1408.4413.

Karner, S.L., Marone, C., 2000. Effects of loading rate and normal stress on stress drop and stick-slip recurrence interval, in: Rundle, J.B., Turcotte, D.L., Klein, W. (Eds.), Geophysical Monograph Series. American Geophysical Union, Washington, D. C.. volume 120, pp. 187–198. URL: http://www.agu.org/books/gm/v120/GM120p0187/GM120p0187.shtml, doi:10.1029/GM120p0187.

Ke, C.Y., 2024. labquake-explorer: Analysis and visualization tools for laboratory earthquake experiments. URL: https://github.com/hueyke/labquake-explorer.

Ke, C.Y., McLaskey, G.C., Kammer, D.S., 2018. Rupture Termination in Laboratory-Generated Earthquakes. Geophysical Research Letters 45, 12784–12792. URL: http://doi.wiley.com/10.1029/2018GL080492, doi:10.1029/2018GL080492.

Ke, C.Y., McLaskey, G.C., Kammer, D.S., 2022. Earthquake breakdown energy scaling despite constant fracture energy. Nature Communications 13, 1005. URL: https://www.nature.com/articles/s41467-022-28647-4, doi:10.1038/s41467-022-28647-4.

Lambert, V., Lapusta, N., Perry, S.M., 2021. Propagation of large earthquakes as self-healing pulses or mild cracks. Nature 591, 252–258. doi:10.1038/s41586-021-03248-1.

Leeman, J.R., Saffer, D.M., Scuderi, M.M., Marone, C., 2016. Laboratory observations of slow earthquakes and the spectrum of tectonic fault slip modes. Nature Communications 7, 11104. URL: https://www.nature.com/articles/ncomms11104, doi:10.1038/ncomms11104.

Liao, Z., Chang, J.C., Reches, Z., 2014. Fault strength evolution during high velocity friction experiments with slip-pulse and constant-velocity loading. Earth and Planetary Science Letters 406, 93–101. URL: http://dx.doi.org/10.1016/j.epsl.2014.09.010, doi:10.1016/j.epsl.2014.09.010.

Lyu, Z., Rivière, J., Yang, Q., Marone, C., 2019. On the mechanics of granular shear: The effect of normal stress and layer thickness on stick-slip properties. Tectonophysics 763, 86–99. URL: https://linkinghub.elsevier.com/retrieve/pii/S0040195119301325, doi:10.1016/j.tecto.2019.04.010.

McLaskey, G.C., 2019. Earthquake Initiation From Laboratory Observations and Implications for Foreshocks. Journal of Geophysical Research: Solid Earth 124, 12882–12904. URL: https://agupubs.onlinelibrary.wiley.com/doi/10.1029/2019JB018363, doi:10.1029/2019jb018363.

Morad, D., Reches, Z., Sagy, A., Hatzor, Y.H., 2024. Energy Dissipation During Shear Along Experimental Rough Faults. Journal of Geophysical Research: Solid Earth 129, e2023JB028605. URL: https://agupubs.onlinelibrary.wiley.com/doi/10.1029/2023JB028605, doi:10.1029/2023JB028605.

Nielsen, S., Spagnuolo, E., Violay, M., Di Toro, G., 2021. Thermal Weakening Friction During Seismic Slip: Experiments and Models With Heat Sources and Sinks. Journal of Geophysical Research: Solid Earth 126, e2020JB020652. URL: https://agupubs.onlinelibrary.wiley.com/doi/10.1029/2020JB020652, doi:10.1029/2020JB020652.

Nielsen, S., Spagnuolo, E., Violay, M., Smith, S., Di Toro, G., Bistacchi, A., 2016. G: Fracture energy, friction and dissipation in earthquakes. Journal of Seismology 20, 1187–1205. URL: http://link.springer.com/10.1007/s10950-016-9560-1, doi:10.1007/s10950-016-9560-1.

Ohnaka, M., Shen, L.f., 1999. Scaling of the shear rupture process from nucleation to dynamic propagation: Implications of geometric irregularity of the rupturing surfaces. Journal of Geophysical Research: Solid Earth 104, 817–844. doi:10.1029/1998jb900007.

Okubo, K., Bhat, H.S., Rougier, E., Marty, S., Schubnel, A., Lei, Z., Knight, E.E., Klinger, Y., 2019. Dynamics, Radiation, and Overall Energy Budget of Earthquake Rupture With Coseismic Off-Fault Damage. Journal of Geophysical Research: Solid Earth 124, 11771–11801. URL: https://onlinelibrary.wiley.com/doi/10.1029/2019JB017304, doi:10.1029/2019JB017304.

Ortega-Arroyo, D., Ghaffari, H.O., Pec, M., Gong, Z., Fu, R.R., Ohl, M., Cattania, C., Plümper, O., 2025. "Lab-quakes": Quantifying the complete energy budget of high-pressure laboratory failure". URL: https://essopenarchive.org/users/528850/articles/1265827--lab-quakes-quantifying-the-complete-energy-budget-of-high-pressure-lab commit=2a35731364e63212995df32831053efc7d961d8f, doi:10.22541/essoar.173884480.00284700/v1.

Paglialunga, F., Passelègue, F.X., Brantut, N., Barras, F., Lebihain, M., Violay, M., 2022. On the scale dependence in the dynamics of frictional rupture: Constant fracture energy versus size-dependent breakdown work. Earth and Planetary Science Letters 584, 117442. URL: https://linkinghub.elsevier.com/retrieve/pii/S0012821X22000784, doi:10.1016/j.epsl.2022.117442.

Palmer, A.C., Rice, J.R., 1973. The Growth of Slip Surfaces in the Progressive Failure of Over-Consolidated Clay. Proceedings of the Royal Society A: Mathematical, Physical and Engineering Sciences 332, 527–548. URL: http://rspa.royalsocietypublishing.org/cgi/doi/10.1098/rspa.1973.0040, doi:10.1098/rspa.1973.0040.

Perry, S.M., Lambert, V., Lapusta, N., 2020. Nearly Magnitude-Invariant Stress Drops in Simulated Crack-Like Earthquake Sequences on Rate-and-State Faults with Thermal Pressurization of Pore Fluids. Journal of Geophysical Research: Solid Earth 125. doi:10.1029/2019JB018597.

Pignalberi, F., Mastella, G., Giorgetti, C., Scuderi, M.M., 2024. Estimating Lab-Quake Source Parameters: Spectral Inversion from a Calibrated Acoustic System. Sensors 24, 5824. URL: https://www.mdpi.com/1424-8220/24/17/5824, doi:10.3390/s24175824.

Poliakov, A.N.B., Dmowska, R., Rice, J.R., 2002. Dynamic shear rupture interactions with fault bends and off-axis secondary faulting. Journal of Geophysical Research: Solid Earth 107. URL: https://agupubs.onlinelibrary.wiley.com/doi/10.1029/2001JB000572, doi:10.1029/2001JB000572.

Samudrala, O., Huang, Y., Rosakis, A.J., 2002. Subsonic and intersonic shear rupture of weak planes with a velocity weakening cohesive zone. Journal of Geophysical Research: Solid Earth 107. URL: https://agupubs.

onlinelibrary.wiley.com/doi/10.1029/2001JB000460, doi:10.1029/2001JB000460.

Scuderi, M., Collettini, C., Viti, C., Tinti, E., Marone, C., 2017. Evolution of shear fabric in granular fault gouge from stable sliding to stick slip and implications for fault slip mode. Geology 45, G39033.1–G39033.1. URL: http://geology.gsapubs.org/lookup/doi/10.1130/G39033.1, doi:10.1130/G39033.1.

Selvadurai, P.A., 2019. Laboratory Insight Into Seismic Estimates of Energy Partitioning During Dynamic Rupture: An Observable Scaling Breakdown. Journal of Geophysical Research: Solid Earth 124, 11350–11379. URL: https://onlinelibrary.wiley.com/doi/10.1029/2018JB017194, doi:10.1029/2018JB017194.

Shreedharan, S., Bolton, D.C., Rivière, J., Marone, C., 2020. Preseismic Fault Creep and Elastic Wave Amplitude Precursors Scale With Lab Earthquake Magnitude for the Continuum of Tectonic Failure Modes. Geophysical Research Letters 47, e2020GL086986. URL: https://agupubs.onlinelibrary.wiley.com/doi/10.1029/2020GL086986, doi:10.1029/2020GL086986.

Svetlizky, I., Albertini, G., Cohen, G., Kammer, D.S., Fineberg, J., 2020. Dynamic fields at the tip of sub-Rayleigh and supershear frictional rupture fronts. Journal of the Mechanics and Physics of Solids 137, 103826. URL: https://doi.org/10.1016/j.jmps.2019.103826, doi:10.1016/j.jmps.2019.103826. arXiv: 1908.10412.

Svetlizky, I., Fineberg, J., 2014. Classical shear cracks drive the onset of dry frictional motion. Nature 509, 205–208. URL: http://www.nature.com/doifinder/10.1038/nature13202, doi:10.1038/nature13202. iSBN: 1476-4687 (Electronic)\r0028-0836 (Linking).

Svetlizky, I., Kammer, D.S., Bayart, E., Cohen, G., Fineberg, J., 2017. Brittle Fracture Theory Predicts the Equation of Motion of Frictional Rupture Fronts. Physical Review Letters 118, 125501. URL: https://link.aps.org/doi/10.1103/PhysRevLett.118.125501, doi:10.1103/PhysRevLett.118.125501.

Tada, H., Paris, P.C., Irwin, G.R., 2000. The Stress Analysis of Cracks Handbook, Third Edition. 3rd ed., ASME, Three Park Avenue New York, NY 10016-5990. URL: http://www.lavoisier.fr/notice/frJZOKO2SEAOHXSR.html, doi:10.1115/1.801535.

Tinti, E., Spudich, P., Cocco, M., 2005. Earthquake fracture energy inferred from kinematic rupture models on extended faults. Journal of Geophysical Research: Solid Earth 110, 1–25. doi:10.1029/2005JB003644.

Udías, A., Madariaga, R., Buforn, E., 2014. Source Mechanisms of Earthquakes: Theory and Practice. 1 ed., Cambridge University Press. URL: https://www.cambridge.org/core/product/identifier/9781139628792/type/book, doi:10.1017/CBO9781139628792.

Vidale, J.E., Houston, H., 1993. The depth dependence of earthquake duration and implications for rupture mechanisms. Nature 365, 45–47. URL: https://www.nature.com/articles/365045a0, doi:10.1038/365045a0.

Viesca, R.C., Garagash, D.I., 2015. Ubiquitous weakening of faults due to thermal pressurization. Nature Geoscience 8, 875–879. URL: http://www.nature.com/articles/ngeo2554, doi:10.1038/ngeo2554. iSBN: 1752-0908.

Wibberley, C.A.J., Shimamoto, T., 2005. Earthquake slip weakening and asperities explained by thermal pressurization. Nature 436, 689–692. URL: http://www.nature.com/articles/nature03901, doi:10.1038/nature03901.

Xia, K., 2004. Laboratory Earthquakes: The Sub-Rayleigh-to-Supershear Rupture Transition. Science 303, 1859–1861. URL: http://www.sciencemag.org/cgi/doi/10.1126/science.1094022, doi:10.1126/science.1094022.